

Defect-Based Fatigue Modeling for AlSi10Mg Produced by Laser Powder Bed Fusion Process



Avinesh Ojha, Wei-Jen Lai, Ziang Li, Carlos Engler-Pinto, and Xuming Su

Abstract Defects are inevitable in metal parts manufactured by any process; the size, shape and location of such defects play a critical role in determining the material's fatigue strength. Due to the random nature of the defects' distribution in the part, a statistical method must be employed for fatigue strength estimation. The laser powder bed fusion (L-PBF) process introduces two main types of porosity defects: keyhole pores and lack-of-fusion pores. A defect-based statistical fatigue strength model has been developed and validated for the L-PBF AlSi10Mg aluminum alloy containing keyhole defects with different size distributions. Artificial defects were also introduced for model validation. The approach is based on the modified Murakami's formulation to address the material dependence and followed the Romano's approach to consider the statistical behavior of the fatigue strength. The proposed model successfully predicts the fatigue strength of different keyhole porosity distributions but is unable to predict the fatigue strength of materials containing lack-of-fusion porosity, possibly due to the higher stress concentration induced by its morphology.

Keywords Fatigue · Defects · AlSi10Mg · Laser powder bed fusion

Introduction

Additive manufacturing (AM) has gained considerable interest in recent years as it offers the possibilities of fabricating near net shape parts with complex geometries that are difficult to build using traditional manufacturing processes. The laser powder bed fusion (L-PBF) process has the advantage over other metal AM processes because of its high-dimensional accuracy and low defect volume. AlSi10Mg is one of the first few aluminum alloys utilized for L-PBF process. It finds a number of applications in the automotive industry, particularly for powertrain components. Since durability is a major concern for such components, understanding the fatigue behavior of L-PBF materials becomes extremely important for successful product design.

A. Ojha · W.-J. Lai (✉) · Z. Li · C. Engler-Pinto · X. Su
Ford Motor Company, 1 America Rd., Dearborn, MI, USA 48121
e-mail: [w lai11@ford.com](mailto:wlai11@ford.com)

© The Minerals, Metals & Materials Society 2021
TMS 2021 150th Annual Meeting & Exhibition Supplemental Proceedings,
The Minerals, Metals & Materials Series,
https://doi.org/10.1007/978-3-030-65261-6_7

There are several important factors that govern the fatigue properties of AM parts, such as surface roughness [1–10], heat treatment [11–13], residual stresses [14–17], and notch effect [18]. Defects such as porosity or inclusions are key factors affecting the fatigue strength of metal AM parts [2, 9, 19–24]. The defect size distribution and morphology depend on powder properties and morphology, processing parameters (such as laser power, scan speed, etc.), and environment (such as gas flow rate). These defects act as microscopic stress raisers, which result in local plastic deformation and can act as crack initiation sites under fatigue loading.

Another important factor that governs the fatigue properties of AM materials is the surface roughness. Surface roughness can be seen as defects with sharp notches and can trigger premature failure under cyclic loading. It has been reported in the literatures that surface roughness decreases the fatigue strength of AM materials by more than 40–50% as compared to the polished surfaces [1–3]. Several models have been proposed to correlate roughness to the fatigue strength reduction, such as the popular empirical model in FKM guideline [25] and the one proposed by Arola [8, 26] based on fatigue notch sensitivity approach, which is able to predict the fatigue strength reduction due to surface roughness

The well-established Kitagawa-Takahashi (KT) diagram [27] and El-Haddad formulations [28] can successfully correlate fatigue strength to defect parameters. One of the widely used models, and perhaps the simplest one, that quantifies the influence of defects and inhomogeneities on the fatigue strength was proposed by Murakami and Endo [29, 30], who found that the fatigue strength corresponds to a threshold stress at which the small cracks do not propagate. The Murakami's approach is based on the Kitagawa-Takahashi diagram, where the threshold stress intensity factor is affected only by the Vickers hardness and the area of the defect projected along the loading direction. The Murakami's equation can be written as

$$\sigma_f = \frac{1.43(120 + HV)}{(\sqrt{\text{area}})^{1/6}} \quad (1)$$

where σ_f is the fatigue strength, HV is the Vickers hardness, and *area* is the area of the defect projected along the loading direction. Note that the Murakami's fatigue strength prediction depends only on two variables: the area of the defect and the hardness value. It is worth noting that Murakami calibrated the model constants (1.43 and 120 in Eq. 1) using fatigue data from many steels and only one wrought aluminum alloy (2017-T4) [31]. The model overestimated the experimental values by approximately 10% for the aluminum alloy [31]. These results indicate that the constants may be material dependent. Another issue is that the model is calibrated using rotating bending fatigue data. Since the fatigue strength measured by rotating bending is always higher than the one measured by uniaxial fatigue testing, the model can significantly overestimate the uniaxial fatigue strength. There are several other studies [32, 33] where new sets of material constants were used to develop and validate Murakami's approach for aluminum alloys. However, none of these models have yet been validated for L-PBF materials. The equations used by Ueno et al. [32] and by Tajirja et al. [33] are shown in Eqs. 2 and 3, respectively.

$$\sigma_f = \frac{1.43(45 + HV)}{(\sqrt{\text{area}})^{1/6}} \quad (2)$$

$$\sigma_f = \frac{1.43(75 + HV)}{(\sqrt{\text{area}})^{1/6}} \quad (3)$$

The current work aims to investigate some preliminary fatigue results and to understand the effect of defects and other material parameters on the fatigue strength of the AlSi10Mg alloy manufactured by L-PBF. This study is critical, as L-PBF alloys have totally different microstructures compared to conventional alloys due to the extremely rapid cooling rate. In addition, the applicability of the defect-based fatigue strength model for L-PBF AlSi10Mg with different defect morphologies (keyhole and lack-of-fusion, LoF) has been investigated. Artificial defects of predetermined sizes were also introduced to generate additional validation points to the proposed modeling approach.

Experimental Procedures

Materials and Sample Preparation

The AlSi10Mg aluminum alloy has been selected for this study. The alloy composition is listed in Table 1. Total four groups of samples (A-D) were produced in this study. Group A and Group B samples were built using the SLM-125 machine by SLM Solutions with the tensile axis in the Z-direction (vertical direction) using optimum process parameters (referred to as “standard” parameters thereafter). An inside-out laser scan strategy was adopted, which melts the center portion first, followed by a contour scan and border scan on the outer part to improve the dimensional accuracy and reduce the surface roughness.

Group A fatigue samples were machined from as-built 15-mm diameter cylindrical rods and then mechanically polished along the axial direction to remove machining marks; these samples are denoted as “MP” (machined and polished).

Two sets of samples were prepared from Group B: one set was machined and polished (MP) and the other set was produced to shape using the L-PBF process (no machining needed) and then mechanically polished to remove the roughness; these samples are denoted as “P” (polished only). The samples were then heat treated at 500°C for 1 hour (solutionizing). Table 2 summarizes the process parameters and heat treatments for these samples.

Groups C and D consist of MP samples built in the horizontal and vertical directions using the SLM-500 machine. These samples were stress relieved at 300°C for 2 hours. Group C uses the standard laser parameters and Group D uses a lower volumetric energy density (VED), which was intentionally optimized to introduce a large amount of LoF defects with the goal to understand the effect of defect morphology on

Table 1 Chemical composition of AISi10Mg aluminum alloy

	Si(%)	Fe(%)	Cu(%)	Mg(%)	Cr(%)	Ni(%)	Ti(%)	Ca(%)	Ga(%)	Sr(ppm)	V(%)	Al(%)
AISI10Mg	10.48	0.125	0.0057	0.291	0.012	0.0108	0.129	0.0059	0.0123	142	0.0146	88.8

Table 2 Summary of process parameters for different groups of fatigue specimens

	Machine	Region	Power (W)	Speed (mm/s)	Hatch spacing (mm)	Layer thickness (mm)	Built plate temperature (°C)	Post heat treatment
Group A (Standard)	SLM 125	Border & Contour	200	730	0.2	0.03	150	N/A
		Hatch	350	1650	0.13			
Group B (Standard)	SLM 125	Border & Contour	330	730	0.2	0.03	150	500°C/1 h
		Hatch	350	1650	0.13			
Group C (Standard)	SLM 500	Border & Contour	300	730	0.17	0.03	200	300°C/2 h
		Hatch	370	1975	0.17			
Group D (Lack of fusion)	SLM 500	Border & Contour	300	730	0.17	0.03	200	300°C/2 h
		Hatch	370	1975	0.17			

the fatigue strength. The laser process parameters were optimized to produce a very small amount of keyhole defects in Group A, B, and C specimens. The LoF defects in Group D specimens are highly irregular with sharp notches along the borders of the defects.

In addition to the naturally occurring defects, drilled holes of different sizes which are larger than the intrinsic defects were introduced in Group A (MP) and Group B (P) specimens. The purpose was to validate the current modeling approach with additional data points. Note that these “artificial defects” resemble keyhole defects in terms of their morphology.

Tensile Test and Hardness Measurement

Tensile tests were carried out in an MTS 100 kN servohydraulic frame for Group A, C, and D samples. The specimen geometry is shown in Fig. 1a, which conforms to ASTM E8 [34]. The displacement rate is 0.19 mm/min up to 1 mm and then 1 mm/min until fracture occurs.

Metallographic samples were cold-mounted to avoid additional heating. Samples were polished; the porosity was measured in the XY-plane; Vickers hardness values were also measured on the same samples using a 300-g force with a dwell time of 13 seconds (5 indentations per specimen).

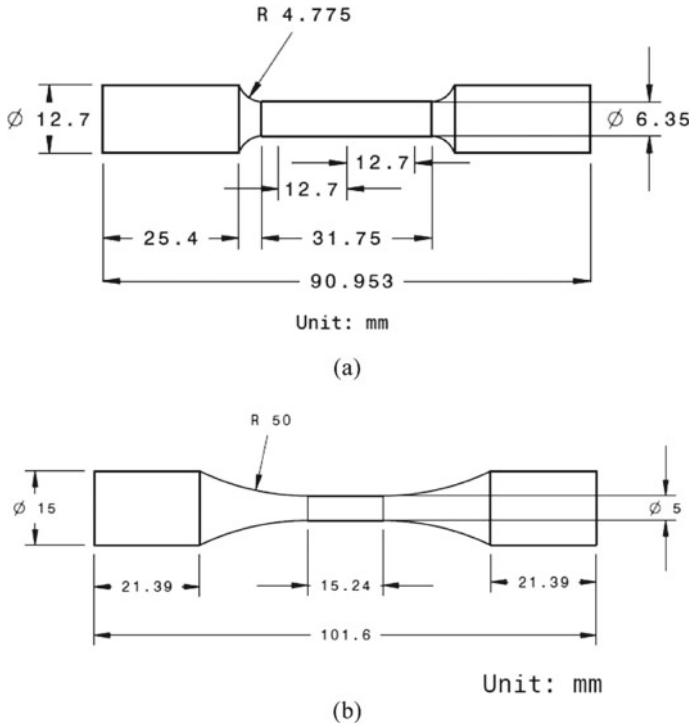


Fig. 1 a Tensile and b fatigue specimen geometries

High Cycle Fatigue (HCF) Test

Fatigue tests were conducted using 100 kN sevohydraulic frames. The specimen geometry follows ASTM E466 [35] and is shown in Fig. 1b. The tests were conducted at a frequency of 70 Hz. The temperature on the specimen surface was monitored during the test using an infrared thermometer. The temperature increase on the specimen surface was limited to $\leq 5^{\circ}\text{C}$ during the test.

Tensile Test and Hardness Measurement

The tensile engineering stress/strain curves are shown in Fig. 2. The average ultimate tensile strength (UTS), yield strength (YS), elastic modulus, elongation to fracture, and Vickers hardness values are provided in Table 3. Mechanical properties of Group A to D specimens. The results are an average of at least three tests for which standard deviations are reported. Table 2. Group A has the highest UTS and YS since it is not post heat treated. The vertical and horizontal samples do not show significant

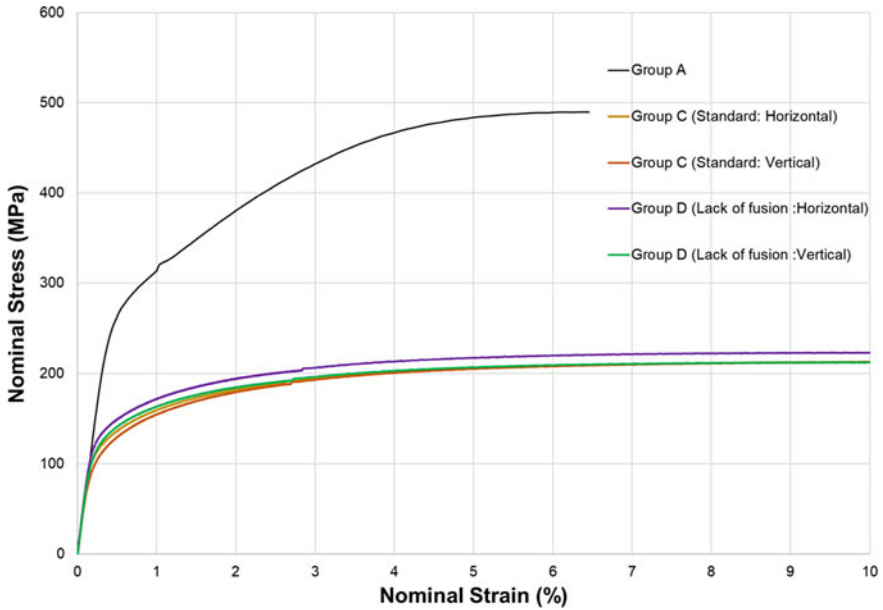


Fig. 2 Average stress/strain curves of Group A-D specimens. Strains up to 10% are shown. (Color figure online)

Table 3 Mechanical properties of Group A to D specimens

	Yield strength (0.2%, MPa)	Elastic modulus (GPa)	Ultimate tensile strength (MPa)	Elongation at fracture (%)	Hardness (HV)
Group A	280.2 ± 1.3	67.1 ± 4.0	491.3 ± 1.8	6.4 ± 0.4	136.6 ± 2.2
Group B	–	–	–	–	67.3 ± 0.7
Group C (Horizontal)	127.5	67.5	212.5	24.8	74.7
Group C (Vertical)	121.3	65.9	210.3	24.2	74.1
Group D (Horizontal)	139.0	70.2	221.4	24.8	78
Group D (Vertical)	135.7 ± 4.4	67.2 ± 1.8	220.5 ± 6.6	20.1 ± 1.9	80 ± 1.3

The results are an average of at least three tests for which standard deviations are reported

difference in Group C and Group D after stress relieving. However, the samples from Group D have slightly higher tensile mechanical properties than the ones in Group C. This might be due to the faster cooling rate associated with the lower VED in Group D.

HCF

Figure 3a, b shows the S-N curves obtained for all groups of specimens (Groups A-D; solid symbols indicate failures and hollow symbols indicate runouts at 10^7 cycles). The method used for fatigue strength calculation needs to consider fatigue behavior of the material tested. Many models have been proposed to fit the fatigue S-N curves; however, these models cannot capture S-N curves near the high-cycle fatigue regime. In the current work, the fatigue strength was calculated using the random fatigue limit (RFL) model [36], which fits the S-N curve using the equation below.

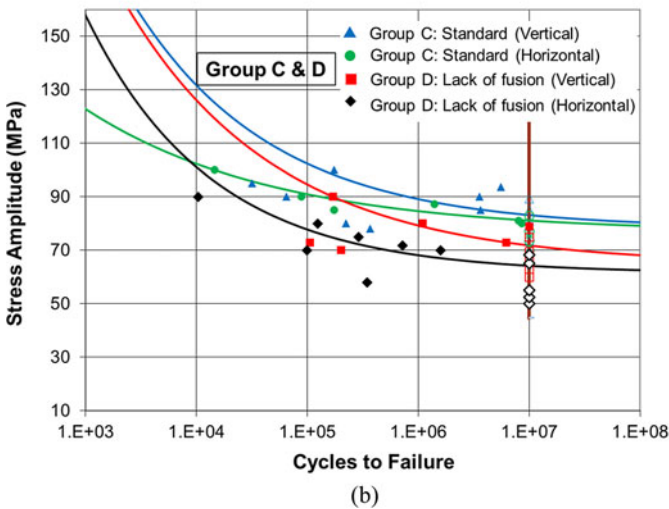
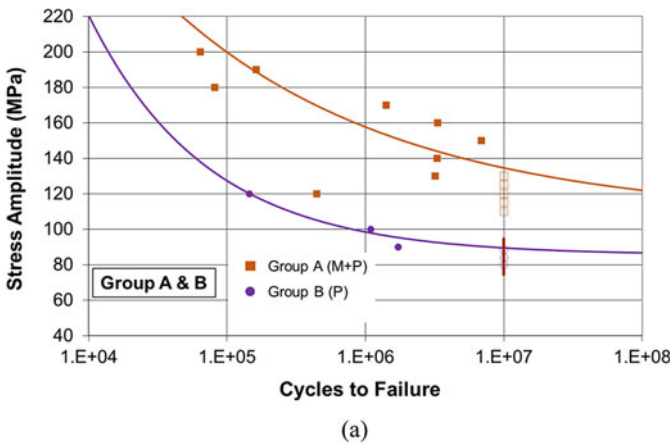


Fig. 3 S-N curves of **a** Group A and B specimens, and **b** Group C and D specimens fitted using RFL method. (Color figure online)

Table 4 Fatigue strengths at 10^7 cycles (and associated standard deviations) obtained from the RFL model

	Fatigue strength (MPa) at 10^7 cycles					
	Group A	Group B	Group C		Group D	
	Vertical	Vertical	Vertical	Horizontal	Vertical	Horizontal
Polished (P)	–	89 ± 2.0	–	–	–	–
Machined & Polished (MP)	133 ± 15.0	–	83.1 ± 10.5	81.1 ± 2.3	71.9 ± 9.3	64.3 ± 6.5

$$S_a - S_L = C(2N_f)^b \quad (4)$$

where S_a is the stress amplitude, S_L is the infinite-life fatigue limit of the material (a random variable following the Weibull distribution), N_f is the number of cycles to fracture, and C and b are empirical constants. In this study, the fatigue S-N curves were fitted using an RFL model with the aid of the maximum likelihood method [37] to account for the runout data points. The model can properly capture the changing slope of the fatigue S-N curves. The fatigue strength distribution is then calculated at 10^7 cycles. The fatigue strength for each group of specimens is provided in Table 4 together with the standard deviation.

Note that the fatigue strength values provided in Table 4 are derived from S-N curves in Fig. 3 which use multiple specimens. Each individual specimen has a different defect distribution and a different fatigue strength; therefore, the fatigue strength reported in Table 4 is the average fatigue strength of all samples tested. Fitting the Murakami's model, on the other hand, requires the fatigue strength to be determined for a single specimen for which the defect area is known. In order to find the fatigue strength of a single specimen, the approach proposed by Maxwell and Nicholas [38] has been followed. According to this approach, a specimen is cycled first at a low stress level (σ_i) until it reaches a pre-determined number of cycles ($N_i = 10^7$ cycles). The specimen is then checked for any microcracks and, if no cracks are detected, the stress level is increased by 5% to σ_{i+1} . This process is continued until the specimen fails at N_{i+1} cycles. The fatigue strength (σ_w) are then estimated using the equation below:

$$\sigma_w = \sigma_i + (\sigma_{i+1} - \sigma_i) \left(\frac{N_{i+1}}{N_i} \right) \quad (5)$$

The major assumption of this method is that there is no significant damage incurred in the specimen at stress levels below the fatigue strength of the material. Therefore, the lives obtained at a higher stress level would not be influenced by the cyclic loading history at the previous lower stress levels. This assumption has been verified and reported in the literature [38].

Figure 4a–c shows the representative micrographs of the fractured surfaces and defect morphologies for Group A–D specimens. The defect from which the fatigue

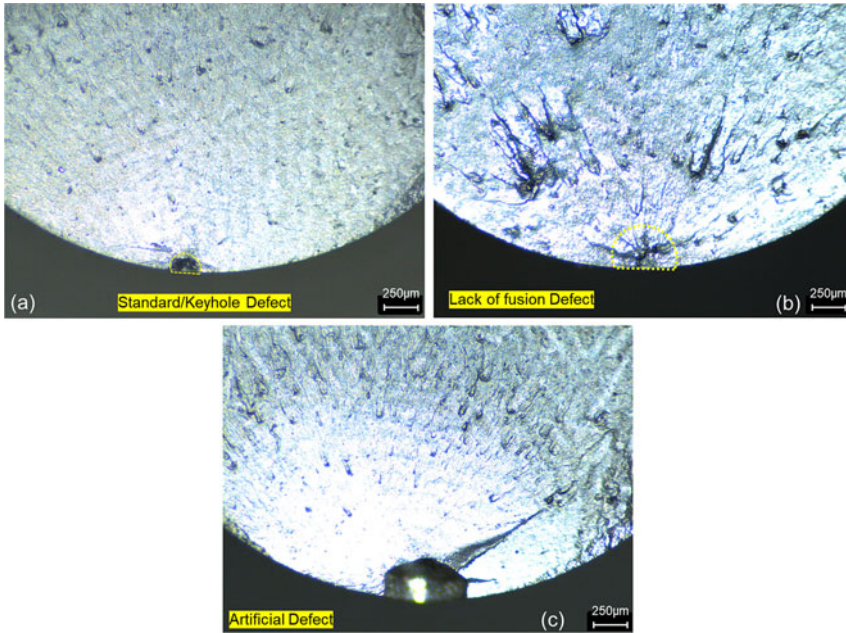


Fig. 4 Optical micrographs showing **a** keyhole defect in Group A (MP) specimen **b** LoF defect in Group D (vertical built) specimen, and **c** artificially introduced defect in Group A (P) specimen. (Color figure online)

crack initiates can be easily identified from the micrographs. The measured areas of the defects are provided in Table 5 with the corresponding fatigue strengths for several tested specimens. The areas were calculated following guidelines described by Murakami [19, 31].

Figure 5 shows the fatigue strength as a function of $\sqrt{\text{area}}$, where $\sqrt{\text{area}}$ is the square root of the measured area of the defect that causes fatigue crack initiation projected in the section perpendicular to the loading direction. The curves in the figure are the Murakami's model predictions for different hardness values. The value of $\sqrt{\text{area}}$ is between 30 and 300 μm for all the specimens considered in the study. To generate additional data for validation, we artificially introduced defects in the specimens by drilling holes in Group A (MP) and Group B (P) specimens. The $\sqrt{\text{area}}$ for these artificial defects is between 400 and 700 μm . These artificially introduced defects are much larger than the naturally occurring ones and fatigue failure originated from these defects is shown in Fig. 4c. The areas of these artificial defects along with their fatigue strengths for all specimens considered in the present study are listed in Table 5. As seen from Fig. 5, Murakami's model prediction using Eq. 3 with modified material constants proposed by Tajiria et al. [33] shows good agreement with the experimental results for different hardness values and areas of the defects for keyhole defects present in Group A to C specimens. However, the model overestimates the fatigue strengths by more than 30% for LoF defect in Group D horizontally built specimens. This is possibly due to higher stress concentration

Table 5 Summary of defect area and experimentally determined fatigue strength for different groups of specimens

	Specimen ID	Build direction	Machining condition	Defect $\sqrt{\text{area}}$ (μm)	Experimental fatigue strength (MPa)
Group A	A1	Vertical	MP	104	147
	A2		MP	57	146
	A3		MP	101	148
	A4		MP	93	140
	A5		MP	114	144
	A6		MP	124	154
	A7		MP	33	111
	A8*		MP	519	106
	A9*		MP	420	119
	A10*		MP	449	109
	A11*		MP	602	100
Group B	B1	Vertical	P	129	81
	B2		P	109	85
	B3*		P	284	73
	B4		MP	33	111
Group C	C1	Vertical	MP	82	92
	C2	Vertical	MP	118	83
	C3	Horizontal	MP	241	80
	C4	Horizontal	MP	163	84
Group D	D1	Vertical	MP	289	72
	D2	Vertical	MP	276	79
	D3	Horizontal	MP	156	69
	D4	Horizontal	MP	261	55

Data with * represents artificially introduced defects

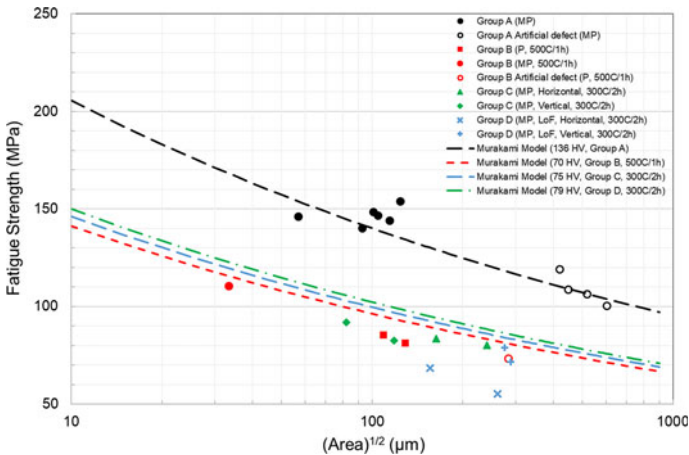


Fig. 5 Fatigue strength as a function of area parameter for different groups of specimens considered in the present study. Dashed lines show Murakami model predictions for different hardness values. (Color figure online)

existing at the irregular LoF defect boundaries. It is worth noting that the measured area of LoF defect on the fracture surface is larger compared to the one of keyhole defect in the specimens. This is in agreement with previous findings in the literature [2].

Probabilistic Approach to Fatigue Strength Prediction

Figure 6a–b shows the micrographs of specimens with keyhole and LoF defects, respectively. The percentage of porosity area is 0.96% and 1.7% for keyhole and LoF specimens, respectively. Note that LoF defects have sharp edges along the borders, which contributes to a higher stress concentration (and lower fatigue strength) than predicted by the current modeling approach. It is well known that defect morphologies can be correlated with the VED [39–42]. The optimal VED for minimizing porosity in AlSi10Mg is between 50–70 J/mm³ based on data reported in the literature [39–42]. VEDs lower than this value will result in lack of fusion defects, and hence lower fatigue strength.

A probabilistic approach is adopted following Beretta and Romano’s work [2, 9, 20, 21] to predict fatigue properties from the measured pore size distribution. This approach assumes that the fatigue crack will initiate from the largest defect near the surface when a given volume of material is subjected to the same cyclic stress. Therefore, the estimation of fatigue strength is based on the probability of finding the largest defect in a given volume of the material. Figure 7a shows the pore size distribution for Group B (P) specimen. The porosity (% area) is 0.85% and the hardness value is 70 HV. Figure 7b shows the corresponding three-parameter Weibull fitting for pores larger than 30 μm (equivalent diameter). The three-parameter Weibull distribution is expressed as

$$f(d) = \frac{\beta}{\eta} \left(\frac{d - \gamma}{\eta} \right)^{\beta-1} e^{-\left(\frac{d-\gamma}{\eta} \right)^\beta} \quad (6)$$

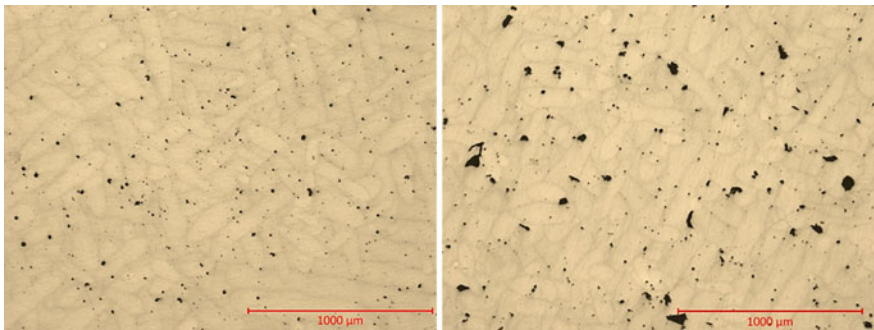


Fig. 6 Defect distribution in specimen with **a** keyhole defects **b** lack of fusion defects. (Color figure online)

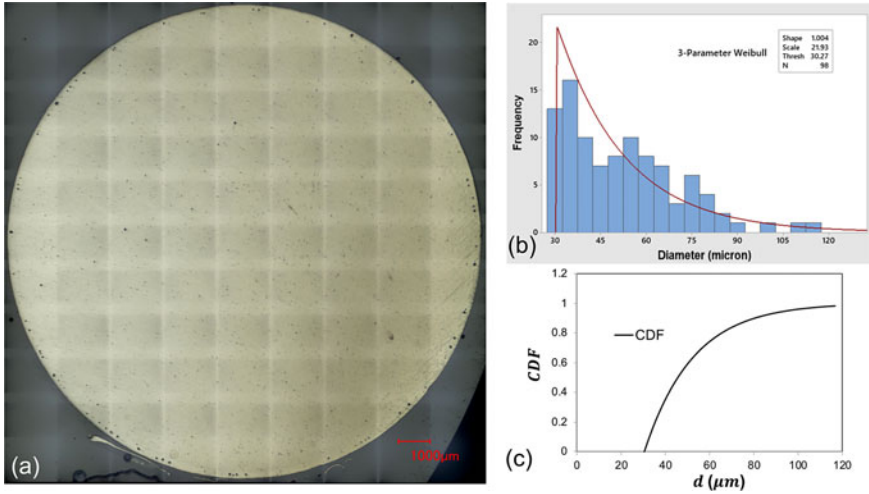


Fig. 7 a A micrograph showing the pore distribution of a Group B (P) specimen. b Probability density function (PDF) and c cumulative distribution function (CDF) of a Group B (P) specimen based on three-parameter Weibull distribution. (Color figure online)

where β, η, γ are the shape, scale, and location parameters, respectively, and d is the equivalent diameter of the pore. The corresponding cumulative distribution function (CDF) is expressed as

$$F(d) = 1 - e^{-(d/\eta)^\beta} \tag{7}$$

Defects smaller than 30 μm in diameter are ignored in the current analysis as that they do not contribute to fatigue failure in most cases. This is also based on the current observation that all fatigue failures initiate from defects which are much larger than 30 μm, as listed in Table 5. Most of the fatigue failures initiate from surface and near-surface pores. Hence only defects within 0.5 mm from the surface are considered and the number density of pores can be estimated by counting the number of pores from the micrograph. Assuming that the pore size distribution is the same in the specimen, the total number of pores in the surface layer of the sample gauge volume is known. Then, the pore size for a given probability $P(\leq d)$ is calculated. The CDF gives the probability of finding a defect smaller than or equal to a certain d and allows us to estimate the fatigue strength of the specimen based on Murakami’s equation. The equations of fatigue strength estimation combining the probabilistic approach and Murakami’s model are shown in Eqs. 8 and 9. Note that the Murakami’s model constants used here are based on the ones used by Tajirja et al. [33]. As shown in Table 6, the predicted fatigue strength of Group B (P) is 88 MPa with the probability $P(\leq d) = 0.5$. This means there is a 50% chance that the fatigue strength of the specimen is above 88 MPa. This value is close to the experimental value of 83 MPa.

Table 6 Summary of fatigue strength predicted using statistical approach

Specimen	Vickers hardness (HV)	Predicted fatigue strength (MPa)	Experimental fatigue strength (MPa)
Group A (MP)	135	120	130
Group B (P)	70	88	83

Similarly, the predicted fatigue strength for Group A (MP) specimen is 120 MPa, which is within 10% of the experimentally obtained value of 130 MPa.

$$\sigma(P(\leq d)) = \frac{1.43(75 + HV)}{\sqrt{\pi \left(\frac{d}{2}\right)^2}}^{1/6} \quad (8)$$

$$d = \eta[-\ln(1 - P(\leq d))]^{(1/\beta)} + \gamma \quad (9)$$

Discussion

One of the important observations in this study is that Murakami's fatigue strength model predicts the fatigue strength quite well for keyhole defects which are rather spherical. However, the fatigue strength prediction for LoF defects has a large deviation from the experimental value. The micrograph shown in Fig. 6b clearly shows that LoF defects are irregular with very sharp notches along the boundaries. However, Murakami [31] reported that fatigue strength is insensitive to defect morphology (based on his experimental observations). Murakami tested samples with drilled holes and cracks with the same defect area in medium carbon steels and the results show very similar fatigue strength. Note that these tests were conducted on conventional alloys which have different microstructure and grain size compared to L-PBF alloys.

Murakami has proposed an effective area concept [19] to calculate the fatigue strength for irregular shaped defect (such the LoF defects observed in L-PBF materials). The effective area is calculated based on defect orientation, distance from the surface, and proximity of one defect to another. The current study used similar guidelines to calculate the effective defect area. However, the model cannot successfully predict the fatigue strength solely based on $\sqrt{\text{area}}$ parameter for materials containing LoF defects. The current results show that defect morphology must also be considered for L-PBF alloys as they are more notch sensitive than conventional cast alloys. This is possibly due to the fine grain structure present in L-PBF alloys [43, 44]. It has been reported that for ultrafine grain alloys, the notch sensitivity factor is even higher than 1 [43]. For this reason, the shape of the defects plays a critical role in dictating the fatigue strength in L-PBF alloys. The modeling of LoF will be considered in a future publication and is beyond the scope of the current work.

In the current study, residual stresses are removed using post heat treatments for Group B, C, and D. The residual stress is removed in Group A during the machining process. The post heat treatment, in addition, also allowed us to investigate the applicability of Murakami's approach by changing the hardness values. It is noted that an increase in hardness value by 10 HV roughly increased the fatigue strength by approximately 7 MPa for the same area of the defect.

Beretta and Romano [2, 9, 20, 21, 24, 45] published a series of papers using El-Haddad's formulation with extreme value statistics to predict the fatigue strength of L-PBF AlSi10Mg. The results show that the fatigue strength is a strong function of the defect size. The use of X-ray CT scan to capture the defect size distribution and defect morphology to correlate mechanical properties is well established. Several authors have discussed this technique, and used the concept of extreme value statistics for a probabilistic approach for fatigue strength prediction [2, 21]. Although the X-ray CT scan provides an accurate information on the defect size distribution, the current study utilizes defect size distribution on a given cross section of the specimen. The assumption is that the process should not affect the defect size distribution from one layer to another and a cross section from any location should be representative of the entire specimen. The current probabilistic approach relies on the concept that only the largest defect at or near the surface of the specimens is considered to cause fatigue failure. The probabilistic approach can successfully predict the fatigue strength within 15% of the experimental value for keyhole defects. This further confirms the applicability of the current modeling approach.

Conclusions

The following conclusions are drawn from the current study.

- (i) The static and fatigue properties of L-PBF AlSi10Mg are obtained for different build orientations and post heat treatments in the current study. The average fatigue strength of specimens containing primarily keyhole defects is slightly higher than the ones containing primarily LoF defects.
- (ii) Fatigue results show that the predicted fatigue strengths based on the Murakami's model are in good agreement with the experimental results for keyhole defects. However, the model cannot be applied to LoF defects.
- (iii) A statistical defect-based model is proposed based on the Murakami's fatigue strength model with modified material constants. The defect-based model can predict the fatigue strength with known defect size distribution of the specimen. The predicted fatigue strengths of L-PBF AlSi10Mg specimen containing keyhole defects are within 15% of the experimental measurement.

References

1. Mower TM, Long MJ (2016) Mechanical behavior of additive manufactured, powder-bed laser-fused materials. *Mater Sci Eng, A* 651:198–213
2. Romano S et al (2017) Qualification of AM parts: extreme value statistics applied to tomographic measurements. *Mater Des* 131:32–48
3. Yadollahi A et al (2018) Fatigue life prediction of additively manufactured material: Effects of surface roughness, defect size, and shape. *Fatigue Fract Eng Mater Struct* 41(7):1602–1614
4. Molaei R, Fatemi A (2019) Crack paths in additive manufactured metallic materials subjected to multiaxial cyclic loads including surface roughness, HIP, and notch effects. *Int J Fatigue* 124:558–570
5. Suraratchai M et al (2008) Modelling the influence of machined surface roughness on the fatigue life of aluminium alloy. *Int J Fatigue* 30(12):2119–2126
6. Mardaras J, Emile P, Santgerma A (2017) Airbus approach for F&DT stress justification of additive manufacturing parts. *Procedia Struct Integrity* 7:109–115
7. Greitemeier D et al (2016) Effect of surface roughness on fatigue performance of additive manufactured Ti–6Al–4 V. *Mater Sci Technol* 32(7):629–634
8. Arola D, Williams C (2002) Estimating the fatigue stress concentration factor of machined surfaces. *Int J Fatigue* 24(9):923–930
9. Beretta S, Romano S (2017) A comparison of fatigue strength sensitivity to defects for materials manufactured by AM or traditional processes. *Int J Fatigue* 94:178–191
10. Pegues J et al (2018) Surface roughness effects on the fatigue strength of additively manufactured Ti–6Al–4 V. *Int J Fatigue* 116:543–552
11. Brandl E et al (2012) Additive manufactured AlSi10Mg samples using selective laser Melting (SLM): Microstructure, high cycle fatigue, and fracture behavior. *Mater Des* 34:159–169
12. Aboulkhair NT et al (2016) Improving the fatigue behaviour of a selectively laser melted aluminium alloy: influence of heat treatment and surface quality. *Mater Des* 104:174–182
13. Zhang C et al (2018) Effect of heat treatments on fatigue property of selective laser melting AlSi10Mg. *Int J Fatigue* 116:513–522
14. Mercelis P, Kruth JP (2006) Residual stresses in selective laser sintering and selective laser melting. *Rapid Prototyping J*
15. Uzan NE et al (2018) On the effect of shot-peening on fatigue resistance of AlSi10Mg specimens fabricated by additive manufacturing using selective laser melting (AM-SLM). *Add Manuf* 21:458–464
16. Leuders S et al (2013) On the mechanical behaviour of titanium alloy TiAl6V4 manufactured by selective laser melting: fatigue resistance and crack growth performance. *Int J Fatigue* 48:300–307
17. Edwards P, Ramulu M (2014) Fatigue performance evaluation of selective laser melted Ti–6Al–4V. *Mater Sci Eng, A* 598:327–337
18. Kahlin M, Ansell H, Moverare J (2017) Fatigue behaviour of notched additive manufactured Ti6Al4V with as-built surfaces. *Int J Fatigue* 101:51–60
19. Masuo H et al (2018) Influence of defects, surface roughness and HIP on the fatigue strength of Ti–6Al–4V manufactured by additive manufacturing. *Int J Fatigue* 117:163–179
20. Romano S et al (2018) Fatigue properties of AlSi10Mg obtained by additive manufacturing: defect-based modelling and prediction of fatigue strength. *Eng Fract Mech* 187:165–189
21. Romano S, Miccoli S, Beretta S (2019) A new FE post-processor for probabilistic fatigue assessment in the presence of defects and its application to AM parts. *Int J Fatigue* 125:324–341
22. Pellizzari M et al (2020) Effects of building direction and defect sensitivity on the fatigue behavior of additively manufactured H13 tool steel. *Theoret Appl Fract Mech* 108:102634
23. Molaei R, Fatemi A (2018) Fatigue design with additive manufactured metals: issues to consider and perspective for future research. *Procedia Eng* 213:5–16
24. Murakami Y, Beretta S (1999) Small defects and inhomogeneities in fatigue strength: experiments, models and statistical implications. *Extremes* 2(2):123–147

25. Forschungskuratorium Maschinenbau e.V. Analytical strength assessment of components in mechanical engineering, FKM guideline (Frankfurt am Main: VDMA, 2003)
26. Arola D, Ramulu M (1999) An examination of the effects from surface texture on the strength of fiber reinforced plastics. *J Compos Mater* 33(2):102–123
27. Kitagawa H (1976) Applicability of fracture mechanics to very small cracks or the cracks in the early stage. *Proc of 2nd ICM, Cleveland*. 1976:627–631
28. El Haddad M, Topper T, Smith K (1979) Prediction of non propagating cracks. *Eng Fract Mech* 11(3):573–584
29. Murakami Y, Endo M (1994) Effects of defects, inclusions and inhomogeneities on fatigue strength. *Int J Fatigue* 16(3):163–182
30. Murakami Y, Endo T (1980) Effects of small defects on fatigue strength of metals. *Int J Fatigue* 2(1):23–30
31. Murakami Y (2019) *Metal fatigue: effects of small defects and nonmetallic inclusions*. Elsevier
32. Ueno A et al (2014) Fatigue limit estimation of aluminum die-casting alloy by means of \sqrt{a} area method. *J Soc Mater Sci, Japan* 63(12):844–849
33. Tajiri A et al (2014) Fatigue limit prediction of large scale cast aluminum alloy A356. *Procedia Mater Sci* 3:924–929
34. ASTM E8 (2001) Standard test methods for tension testing of metallic materials. Annual book of ASTM standards. ASTM
35. ASTM E466 (2003) Standard practice for conducting force controlled constant amplitude axial fatigue tests of metallic materials. Annual Book of ASTM. American Society for Testing and Materials
36. Siebel E, Gaier M (1956) Untersuchungen über den Einfluss der Oberflächenbeschaffenheit auf die Dauerschwingfestigkeit metallischer Bauteile. *VDI-Z* 98(30):1715–1723
37. Engler-Pinto Jr C et al (2005) Statistical approaches applied to fatigue test data analysis. *SAE Trans*, pp 422–431
38. Maxwell DC, Nicholas T (1999) A rapid method for generation of a Haigh diagram for high cycle fatigue. In *Fatigue and Fracture Mechanics: 29th Volume*. ASTM International
39. Read N et al (2015) Selective laser melting of AlSi10Mg alloy: process optimisation and mechanical properties development. *Mater Des (1980–2015)*. 65:417–424
40. Palumbo B et al (2017) Tensile properties characterization of AlSi10Mg parts produced by direct metal laser sintering via nested effects modeling. *Materials* 10(2):144
41. Thijs L et al (2013) Fine-structured aluminium products with controllable texture by selective laser melting of pre-alloyed AlSi10Mg powder. *Acta Mater* 61(5):1809–1819
42. Kempen K et al (2012) Mechanical properties of AlSi10Mg produced by selective laser melting. *Phys Procedia*. 39:439–446
43. Karry R, Dolan T (1953) Influence of grain size on fatigue notch-sensitivity. Illinois Univ at Urbana Engineering Experiment Station
44. Lorenzino P, Navarro A (2015) Grain size effects on notch sensitivity. *Int J Fatigue* 70:205–215
45. Beretta S, Murakami Y (1998) Statistical analysis of defects for fatigue strength prediction and quality control of materials. *Fatigue Fract Eng Mater Struct* 21(9):1049–1065